A non-invasive method for focusing ultrasound through the human skull

G T Clement and K Hynynen

Department of Radiology, Harvard Medical School, Brigham and Women's Hospital,
75 Francis St, Boston, MA 02115, USA

Abstract
A technique for focusing ultrasound through the human skull is described and verified. The approach is based on a layered wavevector-frequency domain model, which propagates ultrasound from a hemisphere-shaped transducer through the skull using input from CT scans of the head. The algorithm calculates the driving phase of each transducer element in order to maximize the signal at the intended focus. This approach is tested on ten *ex vivo* human skulls using a 0.74 MHz, 320-element array. A stereotaxic reference frame is affixed to the skulls in order to provide accurate registration between the CT images and the transducer. The focal quality is assessed with a hydrophone placed inside the skull. In each trial the phase correction algorithm successfully restored the focus inside the skull at a location within 1 mm from the intended focal point. The results demonstrate the feasibility of using the method for completely non-invasive ultrasound brain surgery and therapy.

(Some figures in this article are in colour only in the electronic version)

1. Introduction

The human skull has often been perceived as a barrier to therapeutic ultrasound applications in the brain (Graham-Rowe 1999) due to its strong scattering and attenuating properties. However, early work by Fry *et al* (Fry 1977, Fry and Goss 1980) showed that focusing through the skull at frequencies below 1 MHz is possible. Nonetheless, these foci tended to be shifted and subject to distortion. To compensate for this distortion, Hynynen and Jolesz (1998) adjusted the driving phase of a spherically curved transducer array, using feedback from a hydrophone located at the point of focus. Smith *et al* (1986) and Thomas and Fink (1996) also showed focusing with invasive probes using smaller area arrays suitable for imaging.

To assess the feasibility of using focused ultrasound to perform brain surgery and therapy, previous work has concentrated on three major areas: (i) demonstration that ultrasound can, in fact, be focused through the skull to a reliable location (Thomas and Fink 1996, Hynynen and Jolesz 1998), (ii) investigation into the occurrence of skull heating and heating

This work represents the full version of results originally presented in the Proceedings of the 17th International Congress on Acoustics, Rome, September 2-7, 2001. DOI: 10.13140/2.1.4991.2002

of other regions away from the focus (Clement *et al* 2000), and (iii) achieving a focus intense enough to safely coagulate tissue within a predetermined focal volume (Clement *et al* 2000). To overcome the problem of skull overheating, a hemisphere array design was employed (Sun and Hynynen 1999). The array covered the entire upper surface of the skull in order to distribute the ultrasound energy, thus minimizing the heating. Additionally, the frequency of the array was optimized by examining the power gain ratio between the focus and skull surface as a function of frequency. Both numeric (Sun and Hynynen 1998) and experimental (Clement *et al* 2000) frequency studies revealed a mean optimal frequency of approximately 600–700 kHz for the human skull. Experiments at electrical powers exceeding 2000 W input to the array indicated a momentary temperature rise of approximately 15 °C on the skull surface. This heating is considered acceptable if surface cooling is used to reduce the skin–bone interface temperature before sonication. The functionality of the hemisphere array was demonstrated by producing lesions in tissue through an *ex vivo* human skull.

This past work established that focusing through the skull in a precise location without excessive skull heating is possible. The final step necessary for practical implementation of a trans-skull procedure is a reliable minimally invasive (Tanter *et al* 1998, 2000, Clement and Hynynen 2002) or, ideally, non-invasive (Hynynen and Sun 1999) treatment plan. Our present work concentrates on a non-invasive focusing method that uses CT images to predict how the ultrasound will propagate through the skull. The central problem in the approach lies in predicting the behaviour of the ultrasound field after passing through the skull bone, which causes significant reflection, diffraction and absorption of the field. Successful prediction depends on developing sensible methods and theory. Practical considerations include obtaining accurate knowledge of the thickness and internal structure of the skull bone and precise registration between all points of the skull and the ultrasound array. Theoretical considerations involve finding a model as uncomplicated as possible—keeping the problem computationally feasible—without oversimplification of the problem.

The present algorithm uses thickness, density, and orientation information obtained from CT images of the head. This information is entered into a propagation model, developed in parallel with the present study, which is capable of propagating ultrasound through arbitrarily oriented (non-parallel) layers. Operating in the wavevector-frequency domain, this method rapidly propagates sections of the ultrasound field through the skull. Two specialized cases of the model are examined in the present focusing algorithm. The first case propagates ultrasound through a homogeneous skull with normal incidence. The second considers the angle between the skull surface and the incident acoustic field. Both of these models are tested using *ex vivo* human skulls and hydrophone measurements in a water bath.

2. Theory

A practical trans-skull focusing algorithm must be able to correct for the severe aberration caused by the skull. At the same time the model must be computationally feasible to minimize the treatment planning time for the patient. We have approached the problem using a projection algorithm in the wavevector-frequency domain (Stepanishen and Benjamin 1982). Wavevector propagation methods have substantial computational advantages over both integral and finite-difference methods. While used primarily in homogeneous media (Williams and Maynard 1980, Reibold and Holzer 1985, Fleischer and Axelrad 1986, Christopher and Parker 1991, Liu and Waag 1994, Clement *et al* 1998), wavevector methods easily incorporate the effects of parallel, planar layered media (Schafer 1988, Schafer and Lewin 1989) oriented perpendicular to the propagation axis (Vecchio and Lewin 1994). The present layered approach is applicable to media segmented into an arbitrary number of small regions, and is limited to testing two

approximations. The first model assumes the skull bone is homogeneous and the ultrasound is normally incident upon the skull surface. The second model includes the angle of incidence between the field and the skull.

2.1. Planar propagation

The projection algorithm assumes that the acoustic field satisfies the linearized Stoke's equation,

$$\left(1 + \tau \frac{\partial}{\partial t}\right) \nabla^2 p(\vec{r}, t) = \frac{1}{c^2} \ddot{p}(\vec{r}, t) \tag{1}$$

where τ is the relaxation constant for the medium (Pierce 1989) and c is the real sound speed. While therapeutic arrays operate at high powers, the linear approximation is found to be appropriate for propagation outside of the focus (Hynynen 1991). The highest pressure amplitudes encountered in water before entry into the skull are not expected to exceed 100 kPa, which at 0.74 MHz would correspond to a shock wave parameter of approximately $\sigma = 0.02$ near the skull (Blackstock 1998). Thus, non-linear propagation is not expected to significantly affect the phase prediction algorithm (Zeqiri 1992). A Helmholtz equation in Cartesian coordinates is obtained by the substitution of the Fourier integral

$$\tilde{P}(\vec{r}, t) = \frac{1}{\sqrt[3]{2\pi}} \iint \tilde{p}(k_x, k_y, z, \omega) \, e^{ik_x x} \, e^{ik_y y} \, e^{i\omega t} \, dk_x \, dk_y \, d\omega \tag{2}$$

into equation (1), where the Cartesian wavenumbers are given by k_x and k_y and ω is the angular frequency. The resulting equation,

$$(\nabla^2 + \tilde{k}^2) \tilde{p}(k_x, k_y, z, \omega) = 0 \tag{3}$$

is expressed in terms of a complex wavenumber $\tilde{k}$ given by

$$\tilde{k} = \sqrt{\frac{\omega^2}{c^2} \frac{1}{\sqrt{1 + i\tau\omega}} - k_x^2 - k_y^2}. \tag{4}$$

To propagate the field in a plane at a distance z_0 in front of a source to a new plane z, the advanced solution of equation (3) is used:

$$\tilde{p}(\tilde{k}, z) = \tilde{p}(\tilde{k}, z_0) \, e^{i\tilde{k}(z - z_0)}. \tag{5}$$

In wavevector space, the field recorded in a plane z_0 is thus related to the field at any other plane z by a simple transfer function given in the right-hand side of equation (5). The pressure field in space at z may be obtained by taking the inverse Fourier transform of the equation.

2.2. Rotation

Propagation in wavevector space can be performed using equation (5) after the spatial Fourier transform of the field is calculated for a given plane. In practice, this planar cross section of the field, z_0, is generally chosen to be planar and perpendicular to the propagation axis (Stepanishen and Benjamin 1982). The field can then the projected to an arbitrary new plane z. Such projections have been studied in Cartesian as well as curvilinear coordinates (Wu and Stepinski 1999). Although the transducer considered here is hemispherical, the transducer will be sectioned into small areas that are individually propagated through the skull in a manner that, as described below, yields more easily in Cartesian space. The present case divides the transducer into segments equal to the array's elements (280 mm^2). It is noted that

this does not have to be the case. For example, a large element could be segmented into several smaller elements.

The acoustic pressure in water due to each segment is calculated over a plane located directly above the skull's outer surface. Using the backward projection approach, it is actually more straightforward to first calculate the field of each element at the transducer's geometric focus in water. The field at the focus is calculated using the Rayleigh–Somerfeld integral

$$p_n(\vec{r}, t) = \frac{i\omega\rho}{4\pi} \iint \frac{e^{i(\omega t - k|\vec{r} - \vec{r}'|)}}{|\vec{r} - \vec{r}'|} \vec{v}(\vec{r}') \, d\vec{S}'_n \tag{6}$$

over a planar area 20 mm × 20 mm perpendicular to the geometric centre of the transducer. A water sound speed of $c = 1488$ m s^{-1} and density of $\rho = 1000$ kg m^{-3} is used along with a normalized surface displacement velocity $\vec{v}$. It is noted that this field only needs to be calculated once for a particular transducer, and can be used repeatedly. Alternatively, the effects of imperfections on the array could be added by replacing equation (6) with physical measurements of the field over this area for each element in the array (Clement and Hynynen 2000).

The field due to the nth element is now Fourier transformed giving $\tilde{p}(k_x, k_y, \omega, z_0)$. This planar field is now rotated in the wavevector-frequency domain, defining a new projection plane, z'_0. To visualize this rotation the spatial Fourier transform method, sometimes referred to as the angular spectrum approach, may be viewed as an angular decomposition of the field. That is, each point describes a planar wave with frequency ω passing through the measurement plane at an angle equal to $\alpha_x = \sin^{-1} k_x \frac{c}{\omega}$ from the z-axis in the x–z plane and $\alpha_y = \sin^{-1} k_y \frac{c}{\omega}$ in the y–z plane. The amplitude of the wave is equal to the modulus of $\tilde{p}$. This concept is illustrated in figure 1 for a two-dimensional case. In three dimensions the propagation angles may be expressed in terms of a polar angle θ and azimuthal angle ϕ:

$$\begin{aligned} \tan \alpha_x &= \tan \theta \cos \phi \\ \tan \alpha_y &= \tan \theta \sin \phi. \end{aligned} \tag{7}$$

For a transient signal, each temporal frequency possesses a unique angular spectrum, forming a three-dimensional space consisting of two spatial frequency dimensions and one temporal frequency dimension. Presently, the tested signals are harmonic and may be expressed in two dimensions.

Viewing the wavevector plane as an angular decomposition, it becomes straightforward to perform a passive coordinate rotation. To orient the plane along a new projection axis, z'_0, each point $\tilde{p}$ in wavevector space is mapped to the rotated plane such that

$$\begin{aligned} k_x &\Rightarrow k'_x = \frac{\omega}{c} \sin\left(\alpha_x - \alpha_x^{\text{ROT}}\right) \\ k_y &\Rightarrow k'_y = \frac{\omega}{c} \sin\left(\alpha_y - \alpha_y^{\text{ROT}}\right)' \end{aligned} \tag{8}$$

where α_x^{ROT} is the rotation angle in the x–z plane and α_y^{ROT} is the rotation angle in the y–z plane. In practice these angles are be obtained by inverting the polar and azimuthal orientation of the element using equation (7). Projection along the new axis to an arbitrary new plane z' can be achieved using equation (5). The inverse Fourier transform performed after this mapping provides the pressure field in the plane rotated to $(\theta^{\text{ROT}}, \phi^{\text{ROT}})$, where the spherical polar angles are related to α_x^{ROT} and α_y^{ROT} by equation (7). Trans-skull propagation begins by projecting to the rotated plane at z'_0 to the plane z' directly above the skull's outer surface.

For the physical array, where the exact orientation (θ, ϕ) of the elements is not known *a priori* the projection approach can be used to find their locations. The angles are obtained directly from the Fourier transform of the pressure field, taking angles associated with the maximum amplitude of $\tilde{p}(k_x, k_y, \omega, z_0)$ as the propagation axis.
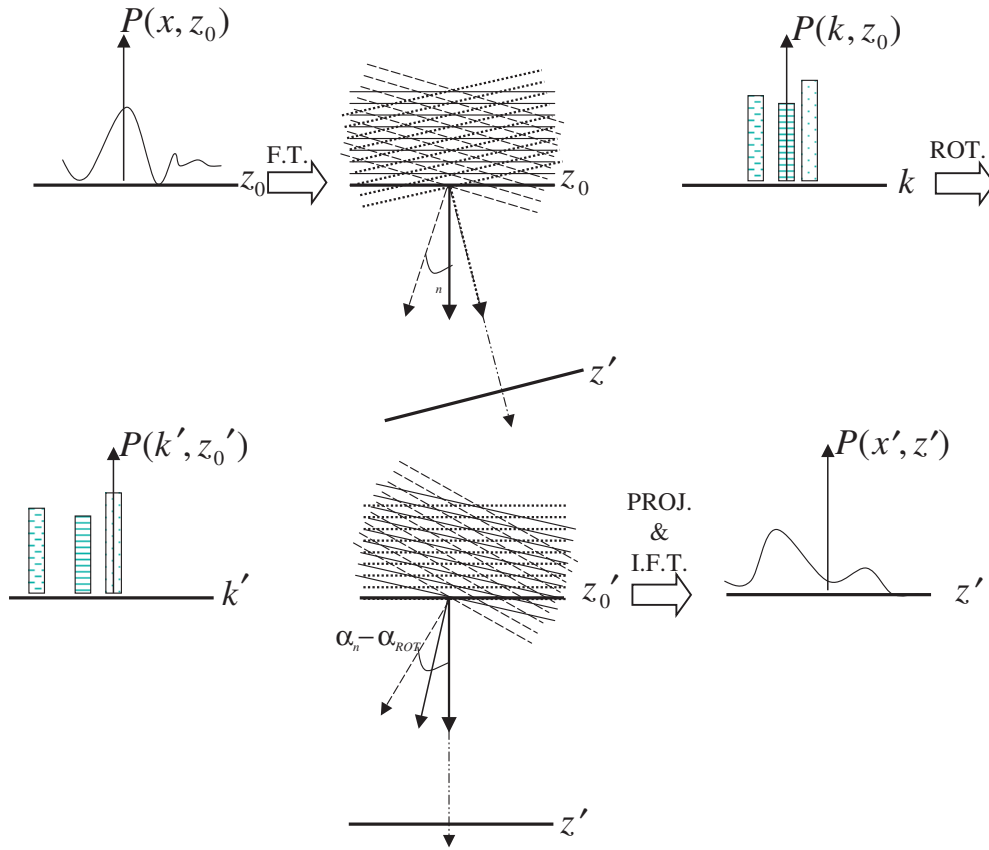
Figure 1. Illustration of the projection method. The field initially at the plane perpendicular to z_0 is rotated and projected to a new plane perpendicular to z'.

2.3. Propagation through layers

After the field is projected to the plane directly above the skull, the angle of incidence is calculated for each wavevector component, $\vec{k}_{xy} = k_x \hat{i} + k_y \hat{j}$, of the pressure. The skull surface directly below the element is approximated as planar by taking the mean vector normal to the surface. This surface is calculated using two vectors on the surface, $\vec{r}_1$ and $\vec{r}_2$, taken using the third nearest neighbouring CT image points in the x- and y-directions. A description of how the surface coordinates are obtained from CT images is provided in the next section.

The scalar product between the wavevector and the cross product of $\vec{r}_1$ and $\vec{r}_2$ provides the incident angle

$$\gamma_{i_{nxy}} = \cos^{-1}\left[\frac{-(\vec{r}_1 \times \vec{r}_2) \cdot \vec{k}_{xy}}{|\vec{r}_1 \times \vec{r}_2||\vec{k}_{xy}|}\right] \tag{9}$$

allowing a transmission angle to be calculated for every component (k_x, k_y) using Snell's law and the pressure transmission coefficient (Kinsler and Frey 1982) for the wavevector component $\vec{k}_{xy}$ through the nth layer,

$$T_{nxy} = \frac{2\rho_{n+1}c_{n+1}\cos\gamma_{i_{nxy}}\cos\gamma_{t_{nxy}}}{\rho_n c_n \cos\gamma_{t_{nxy}} + \rho_{n+1}c_{n+1}\cos\gamma_{i_{nxy}}} \tag{10}$$
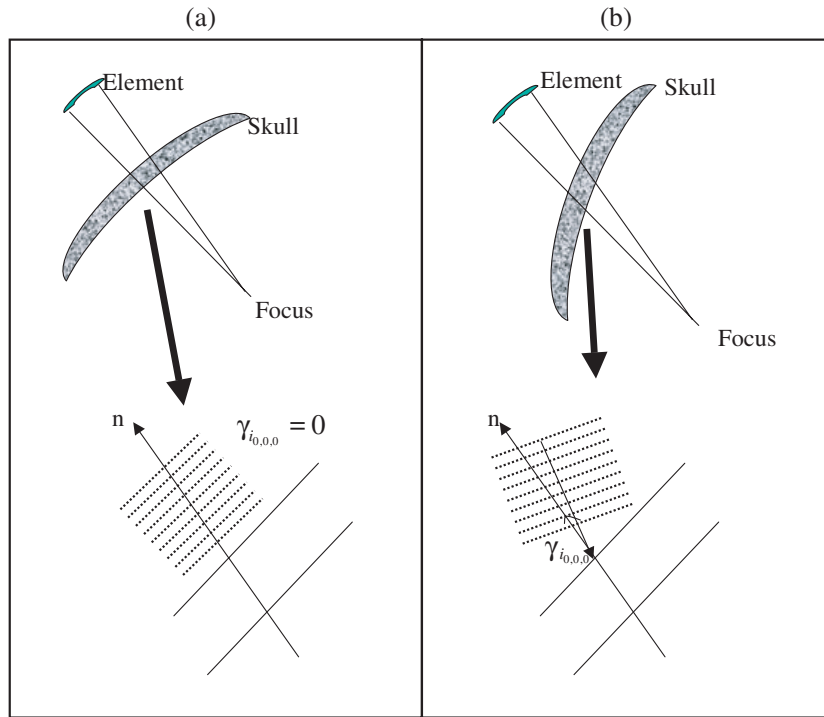
Figure 2. The two propagation cases studied. Case 1 (a) assumes that the ultrasound is incident upon the skull. Case 2 (b) calculates the orientation between the field and the skull surface.

where the outer surface ($n = 0$) is water and the first skull layer ($n = 1$) has a density and sound speed obtained from CT as illustrated in figure 2. The incident and transmitted angles through the nth layer are given by $\gamma_{i_{nxy}}$ and $\gamma_{t_{nxy}}$, respectively.

The problem has now been decomposed into a series of plane waves and the field from the outer surface to the next layer is treated using a ray method. For the case of a skull layer of thickness d, $\tilde{p}(k_x, k_y, \omega)$ of the nth section will vary in phase by

$$\Delta\phi_n = \frac{\omega d_n}{\cos\gamma_{t_{nxy}}} \left(\frac{1}{c_n} - \frac{\cos\left(\gamma_{i_{nxy}} - \gamma_{t_{nxy}}\right)}{c_0} \right) \tag{11}$$

from the field propagated directly through water, as depicted in figure 2(a). If the region is divided into a series of N parallel layers, shown in figure 2(b), the field may be expressed as the summation

$$\Delta\phi = \omega \sum_{n=1}^{N} d_n \frac{1}{c_n \cos\theta_{t_n}} - \phi_0 \tag{12}$$

where ϕ_0 is the ultrasound phase in water if the layers were not present and the transmission angle θ_{t_n} is related to that of the previous layer by the relation

$$\theta_{t_n} = \cos^{-1}\sqrt{1 - \left(\frac{c_n}{c_{n-1}}\right)^2 \left(1 - \cos^2\theta_{t_{n-1}}\right)} \tag{13}$$

given $\theta_{t_0} = \theta_{i_0}$, the incident angle upon the outer skull surface.
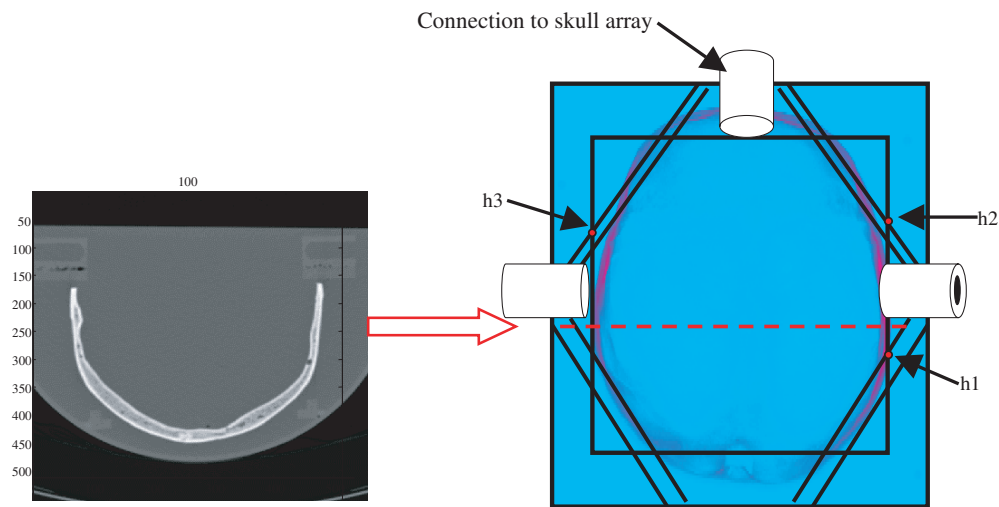
Figure 3. A single CT image (left) is combined to form a 3D image of the skull (right). The image is illustrated around its reference frame showing reference points denoted h_1, h_2, and h_3.

3. Materials and methods

3.1. CT imaging

Information about the shape and structure of each calvarium was obtained by scanning the sample with a Siemens SOMATOM CT Scanner. A bone reconstruction kernel (AH82) was used to acquire image intensities proportional to the bone density. The CT images were taken at 1 mm intervals using a 200 mm × 200 mm field of view, representing a 0.39 mm spatial resolution in the scan plane. A polycarbonate frame was attached around each sample to allow the skulls to be affixed to the array as well as provide a reference for the mechanical positioning system and the CT images, as illustrated in figure 3.

Coordinate points along the inner and outer surfaces of the skull are identified on an image using a threshold filter, which searches for the innermost and outermost densities >1.4 g cm^{-1} along each line of an image. The points of successive images are combined to give a three-dimensional representation of the inner and outer skull surface. Pixel intensities of each image are also combined into a three-dimensional array for later processing.

The phasing algorithm relies on the precise knowledge of the orientation of the skull relative to individual array elements using the CT images. A precision of at least 0.5 mm was achieved, which is of the order of 10% of the ultrasound wavelength inside the skull. To align the skull inside the array, the phasing algorithm translates and rotates the skull data from a CT Cartesian coordinate frame to a coordinate frame stationary with the transducer. The algorithm also translates and rotates the skull from the coordinate frame of the hydrophone measurement system to the transducer coordinate frame. The programme operates using three markers h_1, h_2, and h_3 located at the intersection between reference bars on a polycarbonate frame, which is affixed to the skull (figure 3). These locations may be identified mechanically with the hydrophone positioning system to a precision of approximately 0.1 mm. In the CT images, the 1 mm slice thickness limits the precision along the direction of the scan and makes the precise location of the markers difficult to identify. To circumvent this limit, linear position equations describing each reference point are obtained by identifying two

position vectors $\vec{r}_1$ and $\vec{r}_2$ on the CT images for each reference bar. The position vector of any point on the bar can then be described by

$$\vec{r} = n\frac{\vec{r}_2 - \vec{r}_1}{|\vec{r}_2 - \vec{r}_1|} + \vec{r}_1 \tag{14}$$

where n is an arbitrary scalar. Equating the equations of two intersecting bars and solving for the vector length n describes the point of intersection. It can be shown after algebraic simplification that the intersection occurs when

$$n = \left[(y_2 - y_2')\frac{x_2' - x_1'}{y_2' - y_1'} + x_1' - x_1\right]\left[\frac{x_2 - x_1}{|\vec{r}_2 - \vec{r}_1|} - \frac{y_2 - y_1}{|\vec{r}_2 - \vec{r}_1|}\frac{x_2' - x_1'}{y_2' - y_1'}\right]^{-1} \tag{15}$$

where x, y and x', y' are points in the Cartesian plane of the images with the scan along the Cartesian z-axis.

The programme next generates three rotation matrices that map data points between the transducer, hydrophone and CT coordinate frames. To perform this operation it is necessary to first measure three calibrated reference points, R_1^M, R_2^M, and R_3^M on the array's housing using the mechanical positioning system. Rotation between the hydrophone reference frame and the transducer reference frame is given by

$$R_n^T = \hat{A}_M^T R_n^M \tag{16}$$

where $\hat{A}_M^T$ is the rotation operator, R_n^M represents nth coordinate in the mechanical positioning system frame and R_n^T is the coordinate in the transducer frame. In practice R_3^M is arbitrarily chosen as the point of rotation. Individual rows of the operator, a_i, are obtained by constructing a matrix consisting of rows $\hat{R} = \left[R_n^T\right]_{n=1,2,3}$ and a series of column vectors, $r_x = (x_1, x_2, x_3), r_y = (y_1, y_2, y_3), r_z = (z_1, z_2, z_3)$, where x_1 is the x-component of $\vec{r}_1$, etc, and solving

$$a_i = \hat{R}^{-1} r_i^T. \tag{17}$$

Once $\hat{A}^M$ is known, the translation vector T^M, indicating the geometric centre of the transducer relative to R_3^M is obtained by rotating the known vector in the transducer frame.

Using $\hat{A}_M^T$ the values of the skull reference points h_n^M can be translated and rotated into the the transducer frame. Similarly, a rotation operator $\hat{A}_{CT}^T$ can be obtained to rotate between the CT frame and the transducer frame. Finally, rotation between the CT frame and the mechanical frame is achieved by combining the operators

$$h_n^{CT} = \left[\hat{A}_{CT}^{T-1}\hat{A}_M^T\right]h_n^M. \tag{18}$$

3.2. Registration of array elements

To initially determine the location of the array's elements relative to the reference markers $\left[R_n^T\right]_{n=1,2,3}$ placed on the array, the amplitude and phase of 11 elements were measured in a plane near the geometric centre of the transducer. This field was then rotated using equation (8) and numerically projected backwards with equation (5) to a new plane closer to the array. The peak amplitudes in each plane were identified and their coordinates were used to define the axis of propagation. Minimization of the distances between each of the measured axes determined the coordinates of the geometric centre of the array. A transformation matrix could now be determined for the rotating coordinates between the measurement system's frame of reference and the reference frame of the transducer. The Moore–Penrose pseudo-inverse technique (Boullion and Odell 1971) was used for this process. Here the array coordinates were rotated into element locations specified by the manufacturer (Imasonic, Lyon, France). Using the transformation matrix the location of the reference markers was now known relative to the array elements.

3.3. Skull sound speed

Based on a study of over 1000 measurements performed with ten skulls using a 0.51 MHz transducer, a linear fit of sound speed as a function of skull density was obtained. This linear model, which applies an empirical density correction to the single-layer model, improves the overall correlation with the measured data. A first-order (linear) fit obtained using equation (5) yields the equation,

$$c_{\text{eff}} = 2.06\rho - 1.54 \times 10^3 \, \text{m s}^{-1} \tag{19}$$

in MKS units over the range of thickness-averaged densities between $1.82 \times 10^3 \, \text{kg m}^{-3}$ and $2.45 \times 10^3 \, \text{kg m}^{-3}$. Density measurements obtained by analysing the CT images are inputs to equation (19) to provide the effective skull sound speed values in the focusing algorithm.

3.4. Focusing algorithm

To produce a focus through the skull, the acoustic pressure is calculated at the intended focal point for each element after propagation through the skull. As noted above, two cases are considered. The first case (case 1) ignores incident angles and assumes the ultrasound is incident upon the skull. The second case (case 2) applies equation (9) over the skull surface to include incidence in the model. The pressure phase is compared with the phase expected if the skull were not present. The change in phase caused by the skull is recorded and used for correcting the driving phase of the transducer array. The driving phase of each element is adjusted by an amount

$$\Delta\phi = \arg(P(r)/P_0(r)) \tag{20}$$

where P is the acoustic pressure at the point in the skull and P_0 is the acoustic pressure expected at the same point if the skull were not present. Similarly, a large element could be divided into M sections for propagation, with the driving phase being adjusted by

$$\Delta\phi = \arg\left(\sum_{m=1}^{M} P_m(r)/P_0(r)\right). \tag{21}$$

The entire algorithm was implemented in MATLAB, on a series of Pentium and AMD-based computers over an NT network. A typical processing time for creating a focus within the skull for 320 elements using a 1 GHz machine with 256 MB of RAM is approximately 5 h.

3.5. Experiment procedure

The focusing method was tested on ten formalin-fixed *ex vivo* human skulls. Acoustic properties of the fixed skulls are assumed to be similar to fresh skulls (Fry and Barger 1978). CT images of the skulls were obtained and used in the focusing algorithm, treating the skull bone as homogeneous, so that in equation (12) $N = 3$. Although the wavevector method presented in the theory section is capable of compensating for both the magnitude and phase of the driving signal, only phase correction is considered in the present measurements.

The focusing algorithm generated an ASCII phase file formatted for the custom transducer driving system (Insightec, Haifa, Israel), which contained the transducer driving phases predicted using equation (20). The high power driving system is capable of delivering a maximum of 1800 W of electrical power to 500 channels. The transducer array is a 30 cm diameter, 0.74 MHz hemisphere divided into 500 individual elements. The array was designed in-house and constructed in collaboration with Imasonic (Lyon, France) from a 1–3
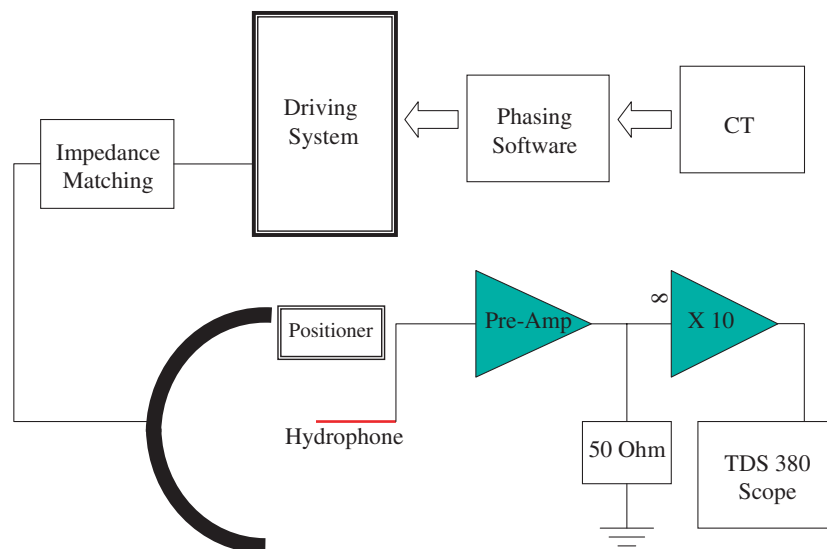
Figure 4. The experimental set-up.

Piezocomposite. Only the lower 320 elements of the array were used for the measurements in order to allow a larger range in the movement of the skull.

Transducer field measurements were conducted in a tank filled with degassed deionized water and padded with rubber to inhibit reflections from the tank walls. A diagram of the set-up is provided in figure 4. Water in the tank was circulated in an effort to produce a uniform temperature throughout the tank. It was assumed that the water temperature remained constant over the measurement period. A 0.2 mm diameter polyvinylidene difluoride (PVDF) hydrophone (Precision Acoustics, UK) was positioned inside the skull and normal to the axis of symmetry of the array. At the driving frequency of 0.74 MHz, the hydrophone directionality is assumed by the classical directional function for circular apertures (Pierce 1989) to amplitude shade all elements by less than -0.01 dB over $90°$. The hydrophone was moved using a stepping-motor-controlled 3D positioning system (Parker, Hannifin, PA). Hydrophone response was sent through a Precision Acoustics pre-amp and recorded by a digital oscilloscope (Textronix, Oregon, Model 380). Both the scan position and the data acquisition were computer controlled. The hydrophone signal was downloaded to a PC and Fourier transformed to obtain the amplitude and phase of the resonant frequency. The acoustic amplitude and phase as a function of position were obtained by measuring a 6×6 mm^2 area at 0.2 mm intervals about a point near the centre of the intended focus. The planar field measurement was used to numerically calculate the field over the entire focal volume using equation (5) to project the measured data to a series of planes 3 mm towards and 3 mm away from the transducer at 0.1 mm intervals. Previous investigations have demonstrated that the fields calculated using this projection method correlate closely with hydrophone measurements (Clement and Hynynen 2000).

Following initial measurement of the acoustic pressure field in water, a skull was attached to the transducer using the reference frame, as illustrated in figure 3, to assure good registration between the skull and the transducer elements. With the hydrophone placed inside the skull the field was measured with all elements driven at the same amplitude and phase. This simulates a situation when no correction is applied for the wave distortion induced by the skull. Next, each

of the non-invasive focusing algorithms was tested separately by phasing the array according to the ASCII phase file it generated and repeating the field measurement. Finally, using feedback from the hydrophone, the phase of each element was adjusted to bring all elements in phase at the array's geometric focus and the field measurement was again performed. This hydrophone measurement provides a reference to compare with the non-invasive models.

Once a focus was obtained with the focusing method, we hypothesized that it was not necessary to implement the algorithm again in order to move the focus. Rather, steering the focus away from the initial focal point was tested using a previously described approach (Clement and Hynynen 2002) where the focus at point r_a was used to calculate the phase necessary to restore a focus at point r_b. In this procedure the phase is adjusted by an amount

$$\Delta\phi(r_b) = \arg\left(\frac{P(r_a)}{P_0(r_a)}P_0(r_b)\right) \tag{22}$$

where measurement (or calculation) of the field in water is given by P_0 and the field with the skull in place is P.

A mechanical shifting of the focus was simulated by repositioning the skull inside the array. Unlike electrical steering, the mechanical case required re-running the entire focusing algorithm for each new focal location. This shifting was performed with two skulls in eight locations placed 6.3 mm apart along the transducer axis of symmetry and in five locations placed 12.5 mm apart along the radial direction normal to this axis.

4. Results

Initially, the 320 elements were powered with the same electrical phase and the resulting field was measured after propagating through each of the *ex vivo* human skull samples. The measurements were taken over a plane normal to the transducer's axis of symmetry at its geometric focus. In each of the ten measurements the fields were observed to experience shifting, distortion, or scattering into multiple foci. Since the voltage output of the hydrophone is proportional to acoustic pressure, the amplitudes of the measurements are squared, to provide a value proportional to the pressure-squared. Since the hydrophone is not calibrated, the response should be regarded as a relative value. Examples of the distortions caused by the skull are shown for two different skulls in figures 5(a) and 6(a). The same measurement plane was then measured once again, but with driving phases determined by the correction algorithm, first neglecting incident angle (figures 5(b) and 6(b)), and then compensating for the incidence (figures 5(c) and 6(c)). To evaluate the success of the non-invasive phase-correcting algorithms, a focus was also obtained using feedback from a hydrophone placed within the skull (figures 5(d) and 6(d)). This hydrophone-phased method assures that the field from each element arrives at the focus in phase and is considered here to be the best field obtainable using the phase correction technique.

To fully evaluate the focal region, the planar measurements were projected over a 512 mm^3 cubic volume using the harmonic projection technique. The projections allowed the location and magnitudes of the peak pressure to be identified. Volumetric slices of the voltage response-squared are shown in figure 7(a) before phase correction and in figure 7(b) after phasing using the algorithm that includes angle of incidence. In the figure, the scattered foci are seen to converge into a single focus after the correction method is introduced, centred less than 0.3 mm from the target location at the graph's origin.

For the ten skulls, the peak signal without phase correction was found to occur at a mean distance of 1.1 mm from the intended focal location with values ranging from 0.45 mm to 2.5 mm and a standard deviation (SD) of 0.64 mm. In seven of the ten cases studied, the
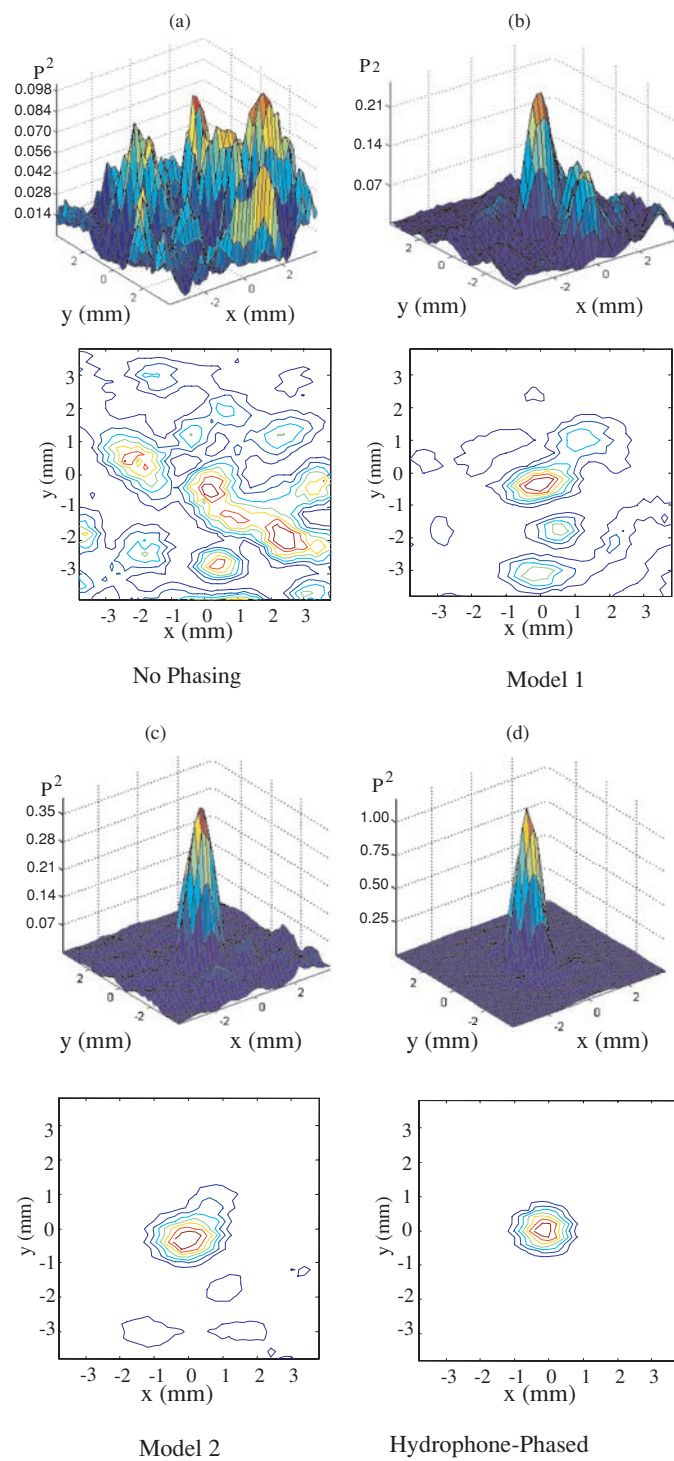
Figure 5. Relative pressure squared near the array's geometric centre: (a) without phase correction, (b) with non-invasive correction using case 1, (c) with non-invasive correction using case 2 and (d) with a hydrophone-assisted focus.

(a)

(b)

No Phasing

Model 1

(c)

(d)

Model 2
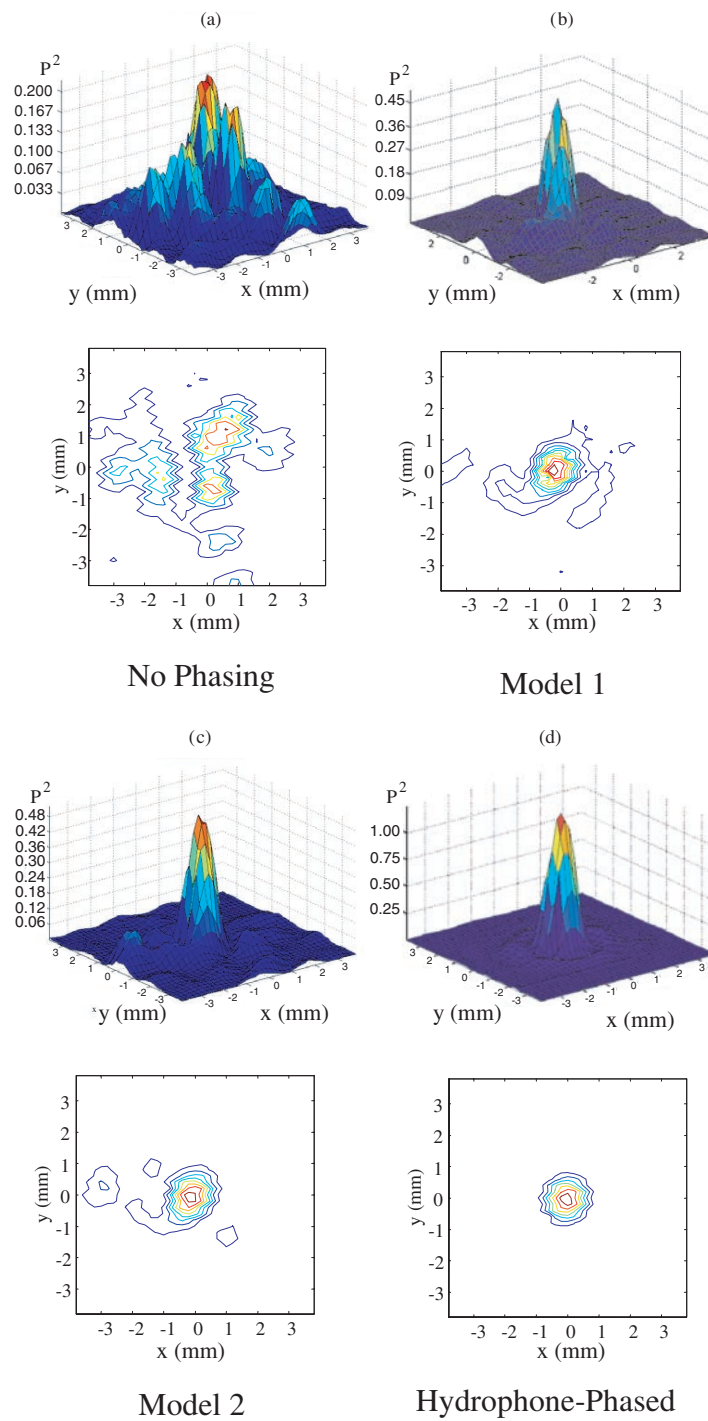
Hydrophone-Phased

Figure 6. A second example of the focus: (a) without phase correction, (b) with non-invasive correction using case 1, (c) with non-invasive correction using case 2 and (d) with a hydrophone-assisted focus.
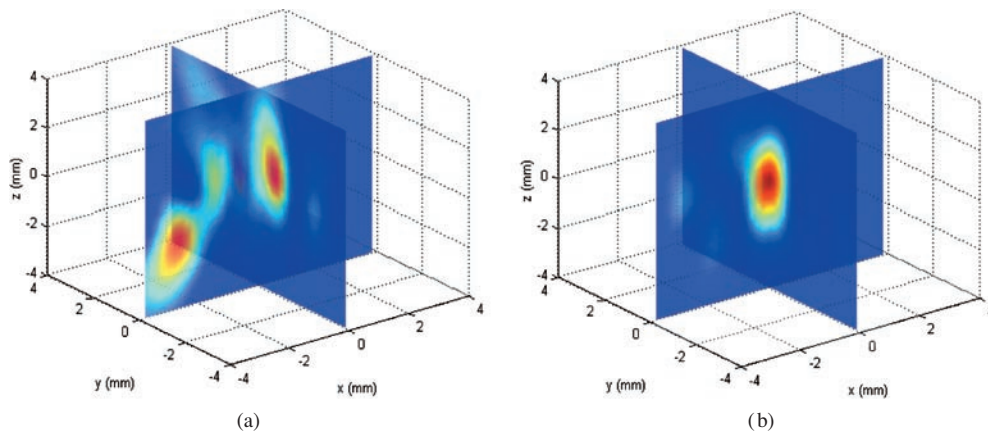
Figure 7. A third example of focusing using case 2 after projecting the planar data over a 3D volume. Field intensities are shown (a) before phase correction and (b) after non-invasive correction.

main focus was scattered into two or more foci, so the peak signal refers to that of the largest (larger) focus. When the phasing algorithm was used, a single focus was always produced, regardless of whether the incident angle was considered. When the phasing algorithm was applied without correction for incident angle, the mean distance from the peak was reduced to 0.59 mm with values ranging from 0.22 mm to 1.1 mm and a SD of 0.26 mm. With the angle of incidence included in the algorithm, the mean distance was further reduced to 0.48 mm over a range of distances from 0.20 mm to 0.82 mm and a SD of 0.22 mm.

The peak voltage-response-squared measurements were also observed to improve with the phasing algorithm. Without phasing, the average peak was found to be 34% of the value obtained by the invasive hydrophone-phasing technique with a variation from 14% to 58% over the samples. The lower amplitudes corresponded to skulls that scattered the field into multiple foci. The phasing algorithm, without correction for incident angle, improved the peak value on average to 46% of the hydrophone-phased signal with a range between 22% and 58%. When the incident angle was included, the average value was 45% with a range from 29% to 59%. The peak values between the two models were, on average, similar. However, the variance was reduced when incident angles were included.

Both models significantly improved the ratio between the peak amplitude and the largest secondary lobes. To assure that all secondary lobes were taken into account, values were obtained from searching within the 512 mm^3 volume obtained using the harmonic projection technique. Without phase correction the secondary peak amplitude averaged 63% of the primary peak. Using the correction algorithm, secondary peaks averaged 29% without angle correction and 32% with the angle included.

Next, the focus was mechanically shifted by moving the skull while keeping the array stationary. In each new location, the array elements were phased with case 2 of the phasing algorithm, which included the effects of the incident angle. Although focusing was achieved at all locations, an increase in the focal peak was observed as a function of the distance from the skull's surface. A plot of 12 locations taken within the skull are shown in figure 8. However, data obtained along the axial direction, represented in the plot by circular points, were found to have higher amplitudes than points taken radially along a line roughly normal to the skull's sagittal suture, and plotted as squares in the figure. Although the amplitude reduced with
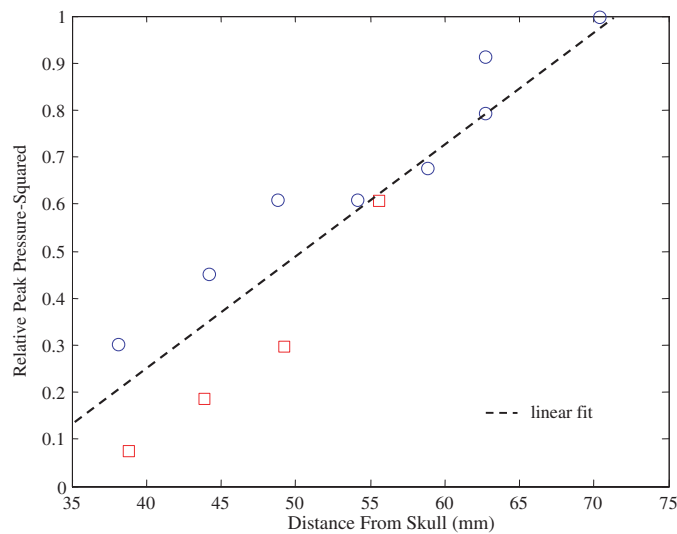
Figure 8. Peak pressure-squared as a function of distance from the skull surface along the transducer's axis of symmetry (circles) and perpendicular to this axis (squares). A linear fit of the data is provided (dashed line).

distance from the skull surface, the shape and location of the focus was observed to remain intact and predictable up to distance of approximately 40 mm from the surface, where larger distortion, secondary lobes and shifting of the focus were observed. Pressure-squared plots for four locations are presented in figure 9.

5. Discussion

Our study was designed to test an algorithm for non-invasive focusing through the human skull. The algorithm relied on several key components developed for the study, including CT-based registration between the skull and the ultrasound transducer, the correlation of sound speed with skull density, and a wavevector-frequency space propagation model. One goal of the study was to simplify calculations in order to expedite focusing. Based on previous measurements with single-element transducers, and with the simplest workable cases in mind, we tested a model that took skull thickness and density into account and a second case that additionally considered refractive effects. In our preliminary investigations we observed a relatively large variation in the effective skull sound speed across a given skull. Since accurate data were required and no suitable tabulated values existed in the literature, we obtained a dataset that was correlated with density. A linear fit of these data was given by equation (19), although a non-linear fit could potentially be obtained to extend the validity of the equation over a wider density range. Both electrical and mechanical beam steering were also explored to extend the focusing range, which would allow large tumour volume to be treated.

Similar to the *ex vivo* study performed here, the application of the technique *in vivo* would require that the patient be affixed to a reference frame before being imaged in a CT scanner. The same frame would then attach to the therapeutic array. In practice the ultrasound must, of course, pass through both skin and brain tissue in addition to the skull bone. Based on previous studies, these tissues are expect to attenuate the signal at the focus, but are not expected to be a major source of beam distortion (Fry and Goss 1980). Since the current study concentrates
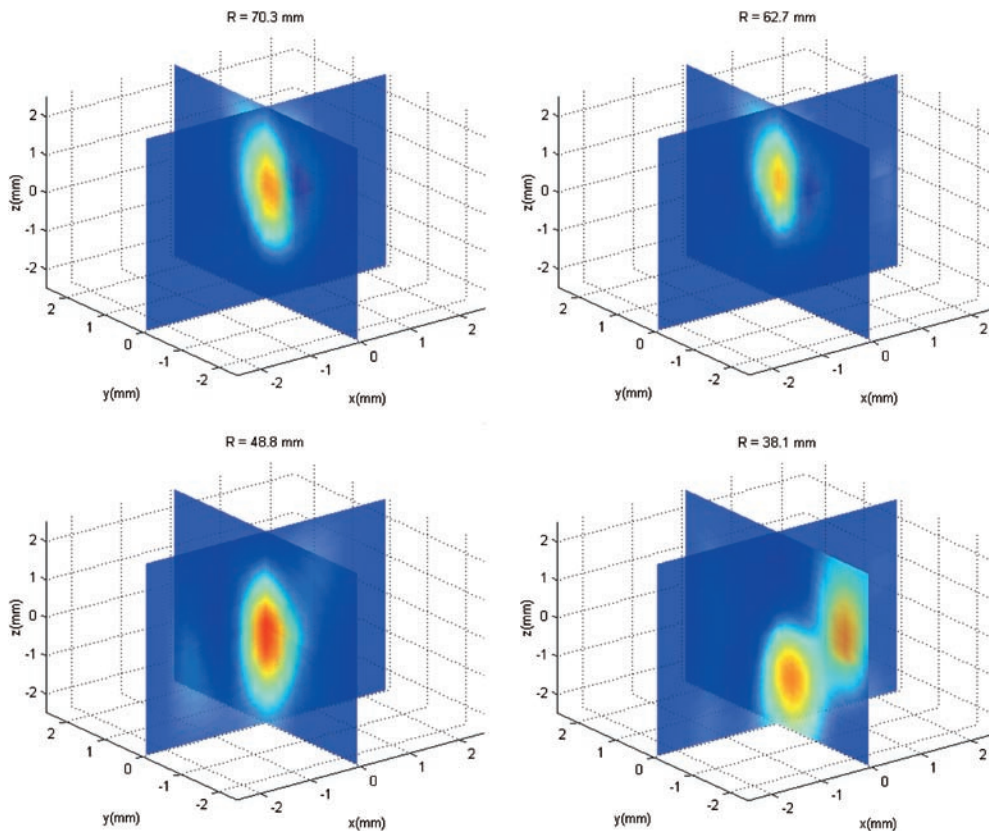
Figure 9. Foci produced using the phasing algorithm at four distances successively closer to the skull surface.

on the restoration of the ultrasound focus, we have simplified the experiment by neglecting these tissues.

The algorithm was first tested under the assumption that the ultrasound wavefront was parallel with the skull. In this case an improvement was observed in the shape, magnitude and location of the focus as compared with an uncorrected beam. The pressure-squared focal peaks were, on average, less than half (46%) the value achieved when hydrophone phasing was used. When the incident angle was added to the algorithm similar intensities were achieved, but with peaks closer (mean = 0.48 mm) to the intended focal point and with lower variance. Overall, the model including angular incidence was 52% higher than the uncorrected case and 51% higher when normal incidence was assumed. With the incident angle considered, the focal location was within 1 mm of the intended focus in each of the ten trials. In both cases, multiple foci present without phase correction converged into a single focus after the algorithm was applied.

The skulls were affixed to their reference frames without regard to the position of the focus within the skull; however, the symmetry of the frame (figure 3) generally resulted in the focus near the centre of the skull. When mechanical shifting was performed, the square of the peak pressure amplitude was observed to increase linearly as a function of the distance from the skull surface. While the precise cause of this drop in amplitude close to the skull is the topic of future work, it is reasonable to expect that the transmission amplitude is a function of

the incident angle upon the skull surface. In the present study, internal refraction effects within the skull resulting from incidence are not taken into account. This is particularly important in the skull, since the bone consists of three distinct regions of inner cortical bone, outer cortical bone and a central trabecular layer. Thus, it may prove that modelling the skull as three or more discrete layers may better compensate for signals at higher incident angles. Amplitude correction will also be considered in order to assure the maximum gain over the entire skull surface regardless of the skull's position within the transducer. Although this mechanical steering may indicate limits based on the single-layer approximation used in this study, it is noted that a focus was still achieved in each of the shifted cases, but with lower amplitudes, as shown in figure 9. Even a low-intensity focus may have significant utility in ultrasound brain therapy when micro-bubbles are injected into the patient to enhance treatment (Hynynen *et al* 2001).

6. Conclusions

This preliminary study demonstrates the ability of a wavevector planar projection model combined with CT image information to construct a focus through the intact skull. The algorithm was effective in restoring a focus in each of the skull samples ($N = 10$) studied. Based on the results of this non-invasive approach combined with the results of past studies involving trans-skull ultrasound at high intensity, we conclude that the algorithm may be used for non-invasive focusing through the human skull for ultrasound therapy. Future work will concentrate on the application of the method at high powers and extension of the method to consider the skull's internal bone layers.

Acknowledgments

References

Blackstock D T 1998 Some model equations of nonlinear acoustics *Handbook of Acoustics* ed M J Crocker (New York: Wiley)
Boullion T and Odell P 1971 *Generalized Inverse Matrices* (New York: Wiley)
Christopher P T and Parker K J 1991 New approaches to the linear propagation of acoustic fields *J. Acoust. Soc. Am.* **90** 507–21
Clement G T and Hynynen K 2000 Field characterization of therapeutic ultrasound phased arrays through forward and backward planar projection *J. Acoust. Soc. Am.* **108** 441–6
Clement G T and Hynynen K 2002 Micro-receiver guided transcranial beam steering *IEEE Trans. Ultrason. Ferroelectr. Freq. Control* **49** at press
Clement G T, Liu R, Letcher S V and Stepanishen P R 1998 Forward projection of transient signals obtainted from a fiber-optic pressure sensor *J. Acoust. Soc. Am.* **104** 1266–73
Clement G T, Sun J, Giesecke T and Hynynen K H 2000 A hemisphere array for non-invasive ultrasound brain therapy and surgery *Phys. Med. Biol.* **45** 3707–19
Fleischer H and Axelrad V 1986 Restoring an acoustic source from pressure data using Weiner filtering *Acoustica* **60** 172–5
Fry F J 1977 Transkull transmission of an intense focused ultrasonic beam *Ultrasound Med. Biol.* **3** 179–84
Fry F J and Barger J E 1978 Acoustical properties of the human skull *J. Acoust. Soc. Am.* **63** 1576–90
Fry F J and Goss S A 1980 Further studies of the transskull transmission of an intense focused ultrasonic beam: lesion production at 500 kHz *Ultrasound Med. Biol.* **6** 33–8
Graham-Rowe D 1999 Zap it and see: could ultrasound reduce the stress of tumour surgery? *New Sci.* **161** 23
Hynynen K 1991 The role of nonlinear ultrasound propagation during hyperthermia treatments *Med. Phys.* **18** 1156–63

Hynynen K and Jolesz F A 1998 Demonstration of potential noninvasive ultrasound brain therapy through an intact skull *Ultrasound. Med. Biol.* **24** 275–83

Hynynen K, McDannold N, Vykhodtseva N I and Jolesz F A 2001 Noninvasive MR image guided focal opening of the blood brain barrier *Radiology* **220** 640–46

Hynynen K and Sun J 1999 Trans-skull ultrasound therapy: the feasibility of using image derived skull thickness information to correct the phase distortion *IEEE Trans. Ultrason. Ferroelectr. Freq. Contr.* **46** 752–5

Kinsler L E and Frey A R 1982 *Fundamentals of Acoustics* (New York: Wiley)

Liu D-L and Waag R C 1994 Correction of ultrasonic wavefront distortion using backpropagation and a reference waveform method for time-shift compensation *J. Acoust. Soc. Am.* **96** 649–60

Pierce A D 1989 *Acoustics, An Introduction to Its Physical Principles and Applications* (Woodbury, NY: Acoustical Society of America)

Reibold R and Holzer F 1985 Complete mapping of ultrasonic fields without the wavelength limit *Acustica* **58** 11–6

Schafer M E 1988 Transducer characterization in inhomogeneous media using the angular spectrum method *Doctoral Thesis* Drexel University

Schafer M E and Lewin P A 1989 Transducer characterization using the angular spectrum approach *J. Acoust. Soc. Am.* **85** 2202–14

Smith S W, Trahey G E and von Ramm O T 1986 Phased array ultrasound imaging through planar tissue layers *Ultrasound Med. Biol.* **12** 229–43

Stepanishen P R and Benjamin K C 1982 Forward and backward projection of acoustic fields using FFT methods *J. Acoust. Soc. Am.* **71** 803–12

Sun J and Hynynen K 1998 Focusing of therapeutic ultrasound through a human skull: a numerical study *J. Acoust. Soc. Am.* **104** 1705–15

Sun J and Hynynen K 1999 The potential of transskull ultrasound therapy and surgery using the maximum available skull surface area *J. Acoust. Soc. Am.* **105** 2519–27

Tanter M, Thomas J-L and Fink M A 1998 Focusing and steering through absorbing and aberrating layers: application to ultrasonic propagation through the skull *J. Acoust. Soc. Am.* **103** 2403–10

Tanter M, Thomas J-L and Fink M A 2000 Time reversal and the inverse filter *J. Acoust. Soc. Am.* **108** 223–34

Thomas J-L and Fink M A 1996 UItrasonic beam focusing through tissue inhomogeneities with a time reversal mirror: application to transskull therapy *IEEE Trans. Ultrason. Ferroelectr. Freq. Control* **43** 1122–9

Vecchio C J and Lewin P A 1994 Finite amplitude acoustic propagation modeling using the extended angular spectrum method *J. Acoust. Soc. Am.* **95** 2399–408

Williams E G and Maynard J D 1980 Holographic imaging without the wavelength resolution limit *Phys. Rev. Lett.* **45** 554

Wu P and Stepinski T 1999 Extension of the angular spectrum approach to curved radiators *J. Acoust. Soc. Am.* **105** 2618–27

Zeqiri B 1992 Errors in attenuation measurements due to nonlinear propagation effects *J. Acoust. Soc. Am.* **91** 2585–93